

Stokes Diagnostics of Wave Propagation in the Magnetic Network on the Sun

G. Vigeesh¹ · O. Steiner² · S. S. Hasan¹

© Springer

Abstract The solar atmosphere is magnetically structured and highly dynamic. Owing to the dynamic nature of the regions in which these magnetic structures exist, waves can be excited in them. Numerical investigations of wave propagation in small-scale magnetic flux concentrations in the magnetic network on the Sun have shown, that the nature of the excited modes depends on the value of plasma β (the ratio of gas to magnetic pressure) where the driving motion occurs. Considering that the properties of these waves should give rise to observable characteristic signatures, we have attempted a study of emergent spectra from our numerical simulations. We find that the signatures of wave propagation in magnetic elements can be detected when the spatial resolution is sufficiently high to clearly resolve magnetic concentrations, enabling observations in different regions within the flux concentrations. The possibility to probe various lines-of-sight around the flux concentration bears the potential to reveal different modes of the magnetohydrodynamic waves and mode conversion. We highlight the feasibility of using the Stokes- V asymmetries as a diagnostic tool to study wave propagation in magnetic structures. These quantities can possibly be compared with existing and new observations in order to place constraints on different wave excitation mechanisms.

Keywords: Magnetic fields, Photosphere; Magnetic fields, Models; Magnetohydrodynamics; Spectral Line, Intensity and Diagnostics; Polarization, Optical; Waves, Magnetohydrodynamic; Waves, Modes

1. Introduction

Spectral lines inform us on the properties of the atmosphere in which they form. In addition, any presence of magnetic fields in the atmosphere modifies the polarization state of the light emerging from the surface. A wealth of information about the structure and dynamics of the magnetized regions of the Sun is hidden in the polarization state of spectral lines. In this paper, we study polarization signatures of wave propagation,

¹ Indian Institute of Astrophysics, Block II Koramangala, Bangalore-560034, India

email: vigeesh@iiaap.res.in email: hasan@iiaap.res.in

² Kiepenheuer-Institut für Sonnenphysik, Schöneckstrasse 6, 79104 Freiburg, Germany
email: steiner@kis.uni-freiburg.de

using numerical simulations. The simulation represent magnetic flux concentrations in the magnetic network on the Sun.

The two dimensional simulations by [Steiner et al. \(1998\)](#) and [Grossmann-Doerth, Schüssler, and Steiner \(1998\)](#) showed that the Stokes profiles vary strongly in response to a dynamic magnetic atmosphere. Using a similar forward modelling, the response of waves on Stokes- V profiles of Ca II infra-red lines were studied by [Pietarila et al. \(2006\)](#). They saw a clear time-dependent behaviour of the Stokes- V profiles as a result of wave propagation and shock formation occuring in the numerically simulated atmosphere. Even though they were able to reproduce the atmospheric dynamics in the form of observational signatures in the Stokes profile, their work was limited to the weak field case. Several authors ([Rosenthal et al., 2002](#); [Bogdan et al., 2003](#); [Cranmer and van Ballegooijen, 2005](#); [Hasan et al., 2005](#); [Hasan and van Ballegooijen, 2008](#); [Khomenko, Collados, and Felipe, 2008](#); [Vigeesh, Hasan, and Steiner, 2009](#); [Fedun, Erdélyi, and Shelyag, 2009](#); [Kato et al., 2011](#)) have investigated wave phenomena in magnetically structured atmospheres. [Shelyag et al. \(2010\)](#) constructed a photospheric bright point model and studied the observational signatures of wave propagation in them including the response in Stokes- V . The effect of a direct excitation of a magnetic flux concentration by granular buffeting and the corresponding spectral signatures of wave propagation and mode coupling and mode conversion in these structures have not been studied so far. [Fujimura and Tsuneta \(2009\)](#) report on the observation of magneto-hydrodynamic waves propagating along magnetic flux tubes in the solar atmosphere. Their work is based on observations with the SOT/SP instrument onboard Hinode space observatory and demonstrates the feasibility of such measurements.

Inspired by the observations and numerical simulations, and driven by the desire to find possible polarimetric signatures of wave propagation in magnetic network elements, we have attempted to study the feasibility of using the analysis of the Stokes- V spectra obtained from our simulation as a diagnostics for magneto-hydrodynamic wave propagation.

The paper is structured as follows: Section 2 gives the construction of the initial equilibrium model. In Section 3, we treat the numerical method and boundary conditions. In Section 4, we present three different experiments of wave propagation in magnetic elements and in Section 5 we discuss the properties of the Stokes profiles emerging from the simulation box. The summary and conclusion are given in Section 6.

2. Initial Equilibrium Model

We construct a two-dimensional initial atmosphere in Cartesian coordinates containing a magnetic flux sheet. For the construction we use the numerical methods described in [Steiner, Pneuman, and Stenflo \(1986\)](#). The magnetic field configuration and the pressure distribution in the physical domain is specified as in [Vigeesh, Hasan, and Steiner \(2009\)](#).

The magnetic field can be written in terms of the flux function $\psi(x, z)$ as

$$B_x = -\frac{\partial\psi}{\partial z}, \quad B_z = \frac{\partial\psi}{\partial x}. \quad (1)$$

Contours of constant flux value, ψ , correspond then to magnetic field lines. We identify $\psi = 0$ with the symmetry axis in the center of the flux-sheet and $\psi = \pm\psi_{\max}$ with

the side boundaries, which also defines the total magnetic flux. The gas pressure is prescribed as a function of height and field line, $p(\psi, z)$, in the following way,

$$p(\psi, z) = \begin{cases} \frac{p(0, z)}{p_0}(p_0 + p_2\psi^2) & \text{if } 0 \leq \psi \leq \psi_1, \\ \frac{p(0, z)}{p_0}(a(\psi - \psi_1)^n + b(\psi - \psi_1)^2 + c(\psi - \psi_1) + d) & \text{if } \psi_1 < \psi < \psi_2, \\ \frac{p(0, z)}{p_0}(p_0 + \frac{B_0^2}{8\pi}) & \text{if } \psi_2 \leq \psi \leq \psi_{\max}, \end{cases} \quad (2)$$

where the constants a , b , c , and d are chosen such that the pressure and its first derivative with respect to ψ is a continuous function of ψ and where we choose $n = 8$. B_0 and p_0 are the magnetic field strength and the gas pressure, respectively, on the axis of the flux-sheet at the reference height $z = 0$. p_2 , ψ_1 , and ψ_2 are chosen conveniently so as to obtain the desired cross-sectional profile for the magnetic field, *viz.*, $B_z(x)$ at $z = 0$, as shown further below in Fig. 3.

The gas pressure along the axis is defined as,

$$p(0, z) = p_0 \exp \left\{ - \int_0^z \frac{\mu g}{RT(z)} dz \right\}. \quad (3)$$

μ is the mean molecular weight, taken to be $\mu = 1.297$, and $T(z)$, the temperature as a function of height, is described by an analytical function of the form

$$T(z) = T_0 + \alpha \tanh(\gamma z + c). \quad (4)$$

It is constant on levels of constant z . With appropriate choice of T_0 , α , γ , and c , we construct a photospheric temperature run as shown in Fig. 1. Initially, the temperature drops rapidly from 10 500 K at the bottom boundary to 6 300 K at $z = 0$ km, then asymptotically decreases to 4 000 K. This temperature profile should approximately reflect the real temperature profile of the photosphere and enable us to compute spectral lines in absorption. We do not include a chromospheric temperature rise because we intend to compute the spectral lines in local thermodynamic equilibrium (LTE) only.

Having defined the gas pressure and the temperature distribution through Eqs. (2)-(4), we obtain the density distribution. From force balance perpendicular to the direction of the field lines, one obtains the electric current density,

$$j_y = \frac{\partial p}{\partial \Psi} \Big|_z. \quad (5)$$

The new magnetic field configuration can be calculated from the current density using the Grad-Shafranov equation,

$$\frac{\partial^2 \psi}{\partial x^2} + \frac{\partial^2 \psi}{\partial z^2} = 4\pi j_y. \quad (6)$$

A detailed derivation of these equations is given in [Steiner \(2007\)](#).

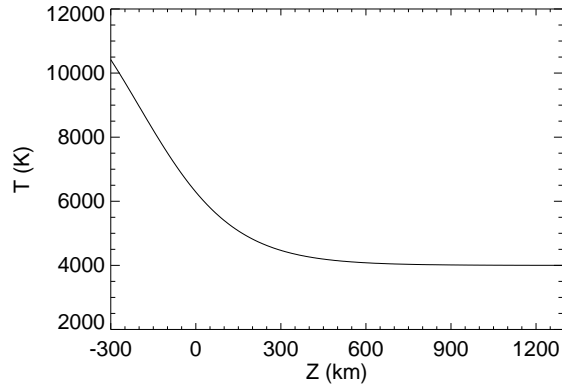


Figure 1. Temperature as a function of height of the model atmosphere, according to Eq. (4) using $T_0 = 9000$ K, $\alpha = -5000$ K, $\gamma = 3 \times 10^{-8} \text{ cm}^{-1}$, and $c = 0.6$. $z = 0$ corresponds approximately to continuum optical depth unity, $\tau_c = 1$, for $\psi = \psi_{\text{max}}$.

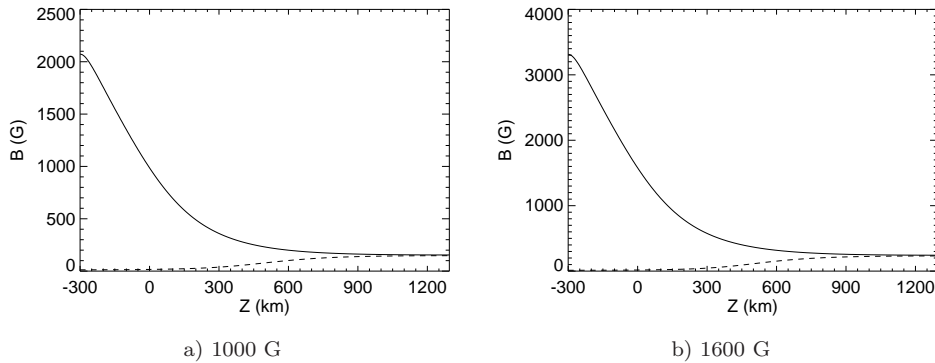


Figure 2. Magnetic field strength as a function of height on the axis (solid curve) and in the ambient medium (dashed curve) of photospheric magnetic flux sheets with field strengths of (a) 1000 G and (b) 1600 G at the axis at $z = 0$.

Due to the symmetry of the problem, we solve Eq. (6) on a computational domain that consists of only half of the flux-sheet of horizontal and vertical extensions of 640 km and 1600 km, respectively. The bottom boundary is at a depth of $z = -300$ km. The domain is discretized on an equidistant rectangular mesh with a spacing of 5 km. The left side of the domain corresponds to the axis of the flux-sheet. The value of ψ is prescribed at the left and the at right side boundaries. At the top and bottom boundaries, we use the Neumann condition $\partial\psi/\partial z = 0$, assuming that the horizontal field component vanishes at these two boundaries. Starting from a reasonable initial field configurations, *e.g.*, as derived from the thin flux-tube approximation, one obtains by iteration of Eqs. (1)-(6), a final, self-consistent, hydrostatic model.

We calculate cases corresponding to different field strengths (at $z = 0$) ranging between 1000 G and 1600 G, on the axis of the sheet. For the case with weaker field strength, the $\beta = 1$ layer lies well above the bottom boundary dropping to a minimum

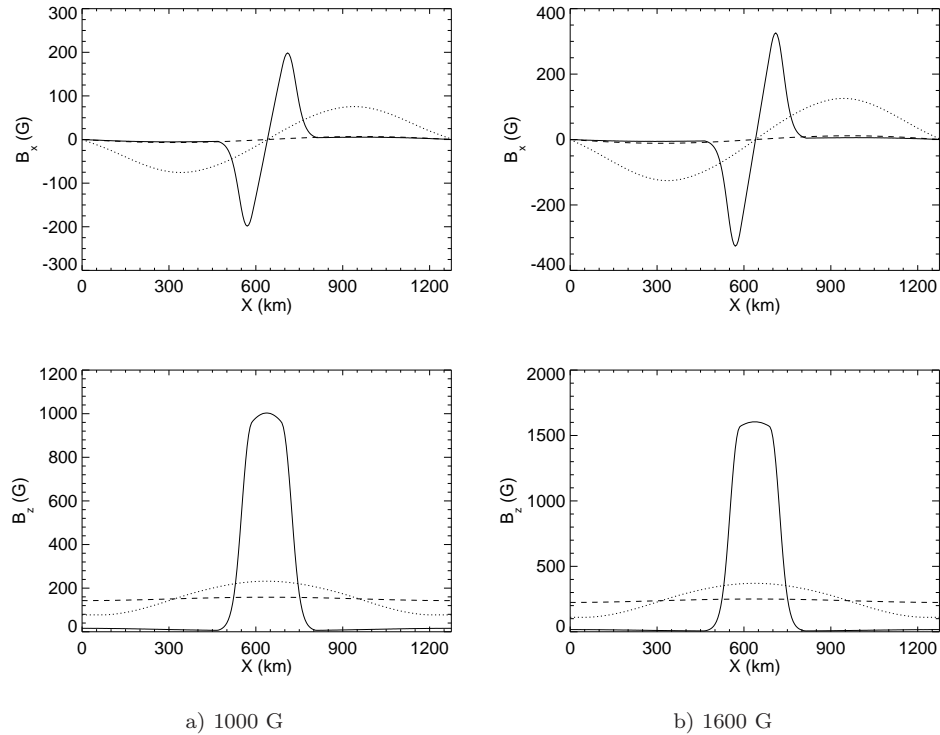


Figure 3. B_x (top row) and B_z (bottom row) components of the magnetic field as a function of horizontal distance at the following heights: $z = 0$ km (solid curve), $z = 500$ km (dotted curve), and $z = 1000$ km (dashed curve). The plots refer to photospheric magnetic flux sheets with field strengths of (a) 1000 G and (b) 1600 G at the axis at $z = 0$.

height of 370 km only. β is the ratio of the gas pressure to the magnetic pressure. Any field line originating from the bottom eventually crosses this layer, dividing the flux-sheet into two regions: a lower region with $\beta > 1$ and the upper region with the $\beta < 1$. We say that the flux-sheet is rooted in a high β region. In the case of a stronger field, *e.g.*, when $B_0 = 1600$ G, the $\beta = 1$ layer traces the boundary of the flux-sheet. The entire flux-sheet is in a region of $\beta < 1$, and only the ambient medium has a high β plasma value.

The variation of the magnetic field strength with height on the axis and in the ambient medium is shown in Fig. 2. In both cases, the magnetic field drops to a uniform value within the flux-sheet. In the ambient medium, the field strength in the lower part is negligible, but with increasing height, it settles down to the same uniform value as that of the flux-sheet. Figure 3 shows the horizontal variation of the horizontal and vertical components of the magnetic field at three different heights, $z = 0$ km (solid curve), $z = 500$ km (dotted curve), and $z = 1000$ km (dashed curve). The horizontal component of the field at $z = 0$ km is close to zero, hence the field is almost vertical at this level. The flux-sheet at this height has a vertical component of the magnetic field that drops sharply to the ambient value in horizontal direction, confining it to a narrow region with a width of about 320 km. The flux-sheet expands with height

Table 1. Equilibrium model characteristics for the 1000 G and 1600 G flux-sheets. The numbers in the first row of each physical quantity correspond to the top boundary ($z = 1300$ km) and the numbers in the second row correspond to the height $z = 0$ km.

Physical quantity	1000 G		1600 G	
	Sheet axis	Ambient medium	Sheet axis	Ambient medium
Temperature [K]	4001	4001	4001	4001
	6342	6342	6342	6342
Density [g cm^{-3}]	7.4×10^{-13}	1.1×10^{-12}	1.7×10^{-13}	1.1×10^{-12}
	2.0×10^{-7}	3.0×10^{-7}	4.5×10^{-8}	3.0×10^{-7}
Pressure [dyn cm^{-2}]	0.2	0.3	0.04	0.29
	8.2×10^4	1.2×10^5	1.8×10^4	12.2×10^4
Sound speed [km s^{-1}]	6.5	6.5	6.5	6.5
	8.2	8.2	8.2	8.2
Alfvén speed [km s^{-1}]	504	394	1672	620
	6.3	0.1	21	0.08
Magnetic field [G]	154	147	243	232
	1003	16	1604	16
Plasma β [-]	2.0×10^{-4}	3.4×10^{-4}	1.9×10^{-5}	1.4×10^{-4}
	2.1	1.3×10^4	0.2	1.2×10^4

to cover the entire horizontal extent with a homogeneous vertical field at a height of $z = 500$ km and above.

The equilibrium characteristics of the two models are summarized in Table 1. The values of the physical quantities are given at the sheet axis and in the ambient medium for the top boundary ($z = 1300$ km) and for the bottom boundary ($z = 0$ km) in the first and second row of each entry, respectively. Note that the plasma β at the sheet axis at the base is 2.1 for the 1000 G case and 0.2 for the 1600 G case. The sound speed (c_s) and the Alfvén speed (v_A) is defined as,

$$c_s = \sqrt{\frac{\gamma p}{\rho}}, \quad (7)$$

$$v_A = \frac{B}{\sqrt{\mu \rho}}, \quad (8)$$

where, p , ρ , and B are the equilibrium values of gas pressure, density and magnetic field strength, respectively.

3. Numerical Simulation: Methods and Boundary Condition

Wave propagation is studied by an impulsive transverse excitation of the lower boundary in the equilibrium model (similar to [Hasan *et al.*, 2005](#) and [Vigeesh, Hasan, and Steiner, 2009](#)). The system of MHD equations, given in conservation-law form for an inviscid adiabatic fluid, is solved according to the method described in [Steiner, Knölker, and Schüssler \(1994\)](#).

The side boundaries are open due to a constant extrapolation of the variables from the physical domain to the boundary cells. The horizontal component of the momentum at the top and bottom boundary and the vertical component at the top boundary are also set by a constant extrapolation. The density in the top and bottom boundary cells is determined using linear log extrapolation. For the temperature, constant extrapolation is used at the top boundary. The temperature in the bottom boundary cells is determined using Eq. (4). The horizontal component of the magnetic field at the top and bottom boundaries are set equal to the corresponding values at the preceding interior point so that $dB_x/dz = 0$. The vertical component of the magnetic field is determined by the condition $\nabla \cdot \mathbf{B} = 0$.

Similar to [Vigeesh, Hasan, and Steiner \(2009\)](#), the transverse velocity V_x at $z = 0$ is specified as follows:

$$V_x(x, 0, t) = \begin{cases} V_0 \sin(2\pi t/P) & \text{for } 0 \leq t \leq P/2, \\ 0 & \text{for } 0 > t > P/2, \end{cases} \quad (9)$$

where V_0 denotes the amplitude of the horizontal motion and P is the wave period. This form simulates an *impulsive* transverse excitation of the flux-sheet at the lower boundary. For simplicity, we assume that all points of the lower boundary have this motion: this does not generate any waves in the ambient medium, other than at the interface with the flux-sheet. In order to achieve significant intensity signals, we use $V_0 = 5 \text{ km s}^{-1}$ and $P = 24 \text{ s}$. Such short duration motions are expected to be generated by the turbulent motion in the convectively unstable subsurface layers, where the flux-sheet is rooted. [Cranmer and van Ballegooijen \(2005\)](#) studied the kinematics of *G*-band bright points and suggested that there are two components involved: a “random walk phase” and a “jump phase”. Our work considers the case with higher velocities, which represents the “jump phase” component of [Cranmer and van Ballegooijen \(2005\)](#). This motion generates magnetoacoustic waves in the flux-sheet.

4. Dynamics

We consider a uniform horizontal displacement of the entire bottom region below $z = 0 \text{ km}$. The excitation corresponds to the *impulsive* case discussed in the Section 3 and given by Eq. (9).

4.1. Moderate Field Case

First we consider the case in which the field strength on the sheet axis is 1000 G (at $z = 0$). The $\beta = 1$ contour in this case is well above $z = 0$ and hence all the magnetic field lines that emerge from the base crosses this layer at some height as is visible from Fig. 4.

The motion of the entire lower boundary region below $z = 0$ (“high- β excitation”) in the direction to the right hand side results in the excitation of waves in the form of a fast (predominantly acoustic) wave and a slow (predominantly magnetic) wave, which propagate at the sound speed and the Alfvén speed, respectively. The fast wave manifests itself as a compression and rarefaction of the gas at the leading and trailing

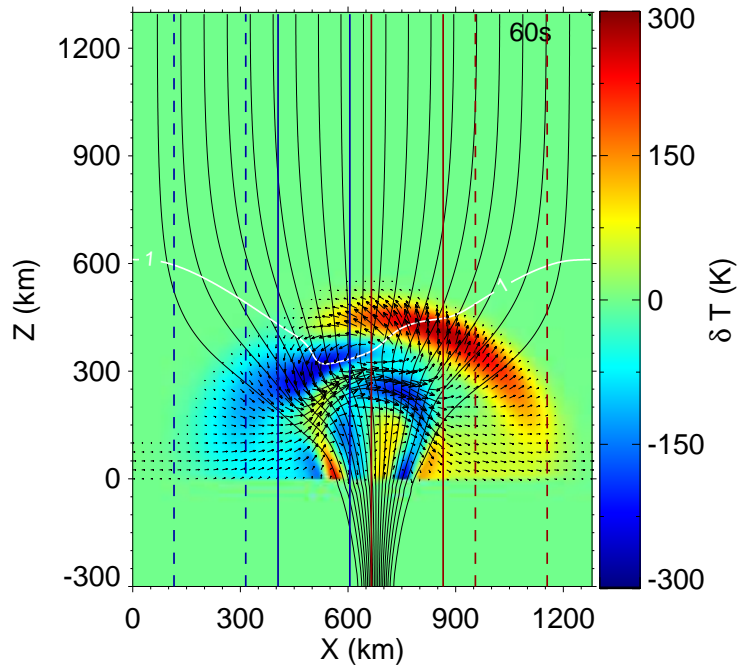


Figure 4. Temperature perturbations and velocity field of a flux-sheet in which the field strength at the axis at $z = 0$ is 1000 G. The snapshot is taken at time 60 s after initiation of an impulsive horizontal motion of the entire region below $z = 0$ km according to Eq. (9). The amplitude of the motion is 5 km s^{-1} and the period $P = 24$ s. The black curves represent magnetic field lines and the white curve depicts the $\beta = 1$ contour. Vertical lines indicate different bundles of lines-of-sight considered for the Stokes analysis.

edge of the flux-sheet, respectively. It can be clearly discerned in the snapshot of the temperature perturbation, δT (the temperature difference with respect to the initial value), shown in Fig. 4 at 60 s after start of the perturbation. The black curves denote the magnetic field lines and the white curve depicts the $\beta = 1$ contour. The perturbations are 180° out of phase on opposite sides of the sheet axis, leading to a quasi anti-symmetric wave pattern. As these fast waves travel upwards they eventually cross the layer of $\beta = 1$, where they change from fast to slow, without changing their acoustic nature: this corresponds to a “mode transmission” in the sense of Cally (2007). The transmission coefficient depends (among others) on the “attack angle”, *i.e.*, the angle between the wave vector and the local direction of the magnetic field (Cally, 2007). On the $\beta = 1$ layer, away from the sheet axis, where the wave vector is not exactly parallel to the magnetic field, we do not have complete transmission of the fast wave to a slow wave. Rather, there is a partial conversion of the mode from fast acoustic to fast magnetic, so that the energy in the acoustic mode is reduced correspondingly. For more details, the reader is referred to Vigeesh, Hasan, and Steiner (2009).

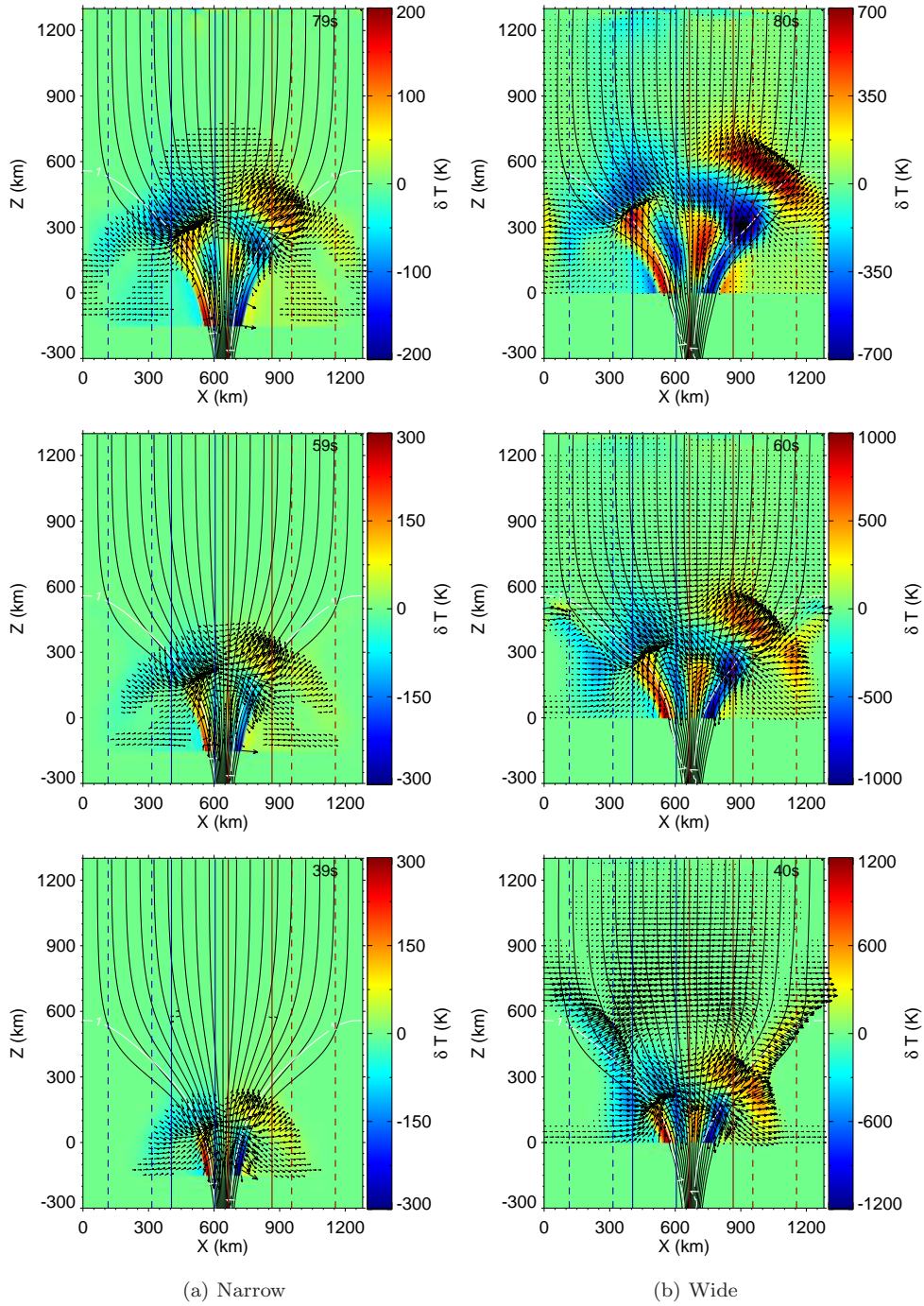


Figure 5. Temperature perturbation for a narrow and a wide excitation depth for a flux-sheet in which the field strength at the axis at $z = 0$ is 1600 G. Time instances refer to 40, 60, and 80 s (from bottom to top) after the initiation of an impulsive horizontal motion in the region from (a) $z = -150$ km and (b) $z = 0$ km to the bottom boundary. The duration of the motion is 12 s and has an amplitude of 750 m s^{-1} . The thin, black, vertically running curves represent field lines and the white curve corresponds to the contour of $\beta = 1$. The arrows indicate velocities of 50 m s^{-1} and more. Vertical lines indicate different bundles of lines-of-sight considered for the Stokes analysis.

4.2. Strong Field Case

We now consider the case in which the field strength on the sheet axis is 1600 G (at $z = 0$). We consider a uniform horizontal displacement of the entire bottom boundary region of a thickness of 150 km (which we term as narrow) and of a thickness of 300 km (wide) from the bottom boundary. This is to mimic the buffeting of the flux tubes by granular eddies of different depths. The excitation corresponds to the impulsive case as given by Eq. (9). Figure 5 shows the temperature perturbation δT at 40, 60, and 80 s for the two cases of narrow and wide region of excitation.

Here, the contour of $\beta = 1$ approximately traces the boundary of the flux-sheet (see Fig. 5). The transverse motion of the lower boundary generates slow (predominantly acoustic) and fast (predominantly magnetic) waves. Since the contour of $\beta = 1$ runs along the boundary of the flux-sheet, waves that travel within the flux-sheet along the magnetic field lines upwards do not encounter this layer and hence do not undergo mode conversion. On the other hand, the fast wave, which can travel across the field, encounters the $\beta = 1$ contour at the boundary of the flux sheet. As the fast wave crosses this boundary, it enters a region of negligible field and hence gets converted into a fast (acoustic) wave as can be seen in the snapshot of temperature perturbations at an elapsed time of 40 s. At this time, the fast wave in the low- β region, which is essentially a magnetic wave, undergoes mode conversion and becomes an acoustic wave, which creates fluctuations in temperature visible as wing like features in the periphery of the flux-sheet (approximately along the $\beta = 1$ contour). The refraction of the fast wave, due to the gradients in Alfvén speed, and the eventual mode conversion is prominent in the case of the wide excitation regime. It can be hardly seen in the case where the flux-sheet is shaken over a narrow region. This is due to the fact that a wide excitation range in a flux tube embedded in a low- β region creates more magnetic pressure fluctuations relative to gas pressure fluctuations and hence imparts more energy to the fast (magnetic) wave. Due to the gradients in Alfvén speed, this mode gets refracted and returns back to a region with high- β , when this energy is transferred to the fast (acoustic) wave, producing larger temperature fluctuations. This has implications for a realistic atmosphere, where granular eddies of different sizes are likely to impact deep rooted flux tubes. An impact over a wide range on a flux tube with strong field will transfer more energy to the fast (magnetic) mode. The ambient atmosphere regains part of this energy in the form of a fast (acoustic) wave due to the refraction of the fast mode and eventual mode conversion. When the excitation range is narrow, there is relatively weak magnetic pressure fluctuation compared to gas pressure fluctuation and hence, most of the energy goes into the slow (acoustic) mode, which is channeled up along the flux tube and eventually dissipates by shock formation.

5. Stokes Diagnostics

Even the largest modern solar telescopes are still not capable of resolving small-scale magnetic structures completely. Observations of the Stokes parameter I cannot reveal properties exclusive to the magnetic feature, since contributions to Stokes- I not only come from the magnetic field but also from the surrounding field-free or weak-field plasma. Differently from that, Stokes- V gives us the properties exclusive to

the magnetic structures, because the circularly polarized light is formed only where the magnetic field is present. So the most sensitive method to study the magnetic atmosphere is by analysing the Stokes- V spectra emerging from them (see [Sigwarth \(2000\)](#) for a review).

Table 2. Atomic parameter of the selected lines.

Ion	Wavelength (Å)	Excitation Potential (eV)	$\log(gf)$	g_{eff}	Lower Level	Upper Level
Fe I	5250.21	0.121	-4.938	3.0	5D_0	7D_1
Fe I	5247.05	0.087	-4.946	2.0	5D_2	7D_3
Fe I	6301.50	3.654	-0.718	1.67	5P_2	5D_2
Fe I	6302.49	3.686	-1.235	2.5	5P_1	5D_0

Values taken from [Nave et al. \(1994\)](#).

We have computed the emergent Stokes- V profiles from the top of our simulation box for the case of flux-sheets with field strengths of 1000 G and 1600 G, using the Stokes radiative transfer code DIAMAG ([Grossmann-Doerth, 1994](#)). This code calculates the normalized Stokes parameters by solving the Unno-Rachkovsky equations of radiative transfer. At the same time, it computes the line depression contribution function for each wavelength point. The program requires the temperature, gas pressure, magnetic field vector, velocity, and micro-turbulence to be specified on every grid point along the line of sight (LOS). The calculations were done for a set of four Fe I lines, *viz.*, $\lambda\lambda$ 5250.2, 5247.05, 6301.5, and 6302.5 Å. The atomic parameters of the selected lines are listed in Table 2.

Table 2 lists the wavelengths of the lines, the excitation potentials of the lower level, oscillator strengths ($\log(gf)$), and the effective Landé g -factors (g_{eff}). The two pairs of lines were selected because each forms under similar conditions in the atmosphere, since the lines of each pair have similar excitation potentials and oscillator strengths, which means similar opacities. But the difference in Landé g -factor for these lines make them useful for measuring the magnetic field strength, in particular, deviations from the weak field regime. These lines are commonly used to study solar magnetic fields. [Socas-Navarro et al. \(2008\)](#) have confirmed the reliability of using these four lines for the diagnostics of the quiet Sun magnetic field.

Here we study the spectral signature of wave propagation in magnetically structured atmospheres with dynamically varying magnetic field. The effects of wave propagation in the four Fe I lines, listed in Tab. 2 are assessed, using the numerical simulations described in Section 4. The Stokes spectra for vertical lines-of-sight, separated by a horizontal distance of 10 km, were computed for each time step. These correspond to real observations at disk center. Here, we present the analysis of the Stokes- V spectra for the two cases of moderate and strong magnetic field.

The Stokes- V profiles were computed along vertical lines-of-sight by integration of the radiative transfer equation for polarized light. If the profiles emerging from the top boundary are spatially averaged over the entire width of the box, the profiles do not show significant variation with time revealing no sign of wave propagation inside the

box. This is due to the fact that the antisymmetric flow pattern within the flux-sheet will average out to give zero net contribution to the Stokes- V variation. This is different in the case when the horizontal integration is carried out over only a narrow spatial window on either side of the flux-sheet axis. In this case, profiles show signatures of wave propagation. Therefore, it is necessary to observe at very high spatial resolution in order to study the effect of wave propagation in individual flux concentrations. Lines-of-sight that cover only one half of the flux-sheet or a small part of it give more information about the wave activity in the domain. In order to quantitatively study the signatures of wave propagation, we study the evolution of the wavelength shift of the central zero crossing of Stokes- V ($\delta\lambda_{zc}$) and the area and amplitude asymmetries, δA and δa , respectively, according to Eqs. (10)-(12). The zero-crossing shift of Stokes- V is defined as,

$$\delta\lambda_{zc} = \lambda_{zc} - \lambda_0, \quad (10)$$

where λ_{zc} is the wavelength of the central zero-crossing of the Stokes- V profile and λ_0 a reference wavelength, which for the present purpose is the rest wavelength of the spectral line. The asymmetries between the blue and red lobe areas of the Stokes- V profiles, A_b and A_r and the amplitudes of the blue and the red lobe, a_b and a_r are defined as,

$$\delta A = \frac{|A_b| - |A_r|}{|A_b| + |A_r|}, \quad (11)$$

and

$$\delta a = \frac{|a_b| - |a_r|}{|a_b| + |a_r|}. \quad (12)$$

5.1. Moderate Field Case

Figures 6 and 7 show snapshots of Stokes- V profiles of Fe I $\lambda\lambda$ 5250.2, 5247.06, 6301.5, and 6302.5 Å, at time $t = 40$ s after the start of the simulation of the moderate field case (see Fig. 4 for reference). Figure 6 shows the Stokes- V profiles averaged over a horizontal distance from $x = 410$ km to $x = 610$ km (left of the symmetry axis) and Fig. 7 shows the profiles averaged over $x = 670$ km to $x = 870$ km (right of the symmetry axis). The lines Fe I λ 5250.2 Å and Fe I λ 5247.06 Å belong to the same multiplet of iron, differing only in the effective Landé g -factor, which are 3 and 2, respectively. Hence, the Stokes- V amplitudes are different for the two lines and scale approximately according to the ratio given by the Landé g -factor as 3:2. This can be seen in the plots shown in Fig. 6, where the amplitude of Fe I λ 5247.06 Å is lower than that of Fe I λ 5250.2 Å. Similarly, the amplitudes of Fe I λ 6301.5 Å and Fe I λ 6302.5 Å scale according to the Landé g -factors of 1.67 and 2.5, respectively. However, the amplitude ratios are not strictly according to the Landé g -factor ratios in the strong-field regime because of saturation effects (Stenflo, 1994).

The height of formation of the spectral lines depends on the line strength, which in turn depends on the excitation potential and the log (gf). The region of formation spans a wide range and is affected by the presence and the height variation of the magnetic field—the latter matters in particular for Stokes parameters Q , U , and V .

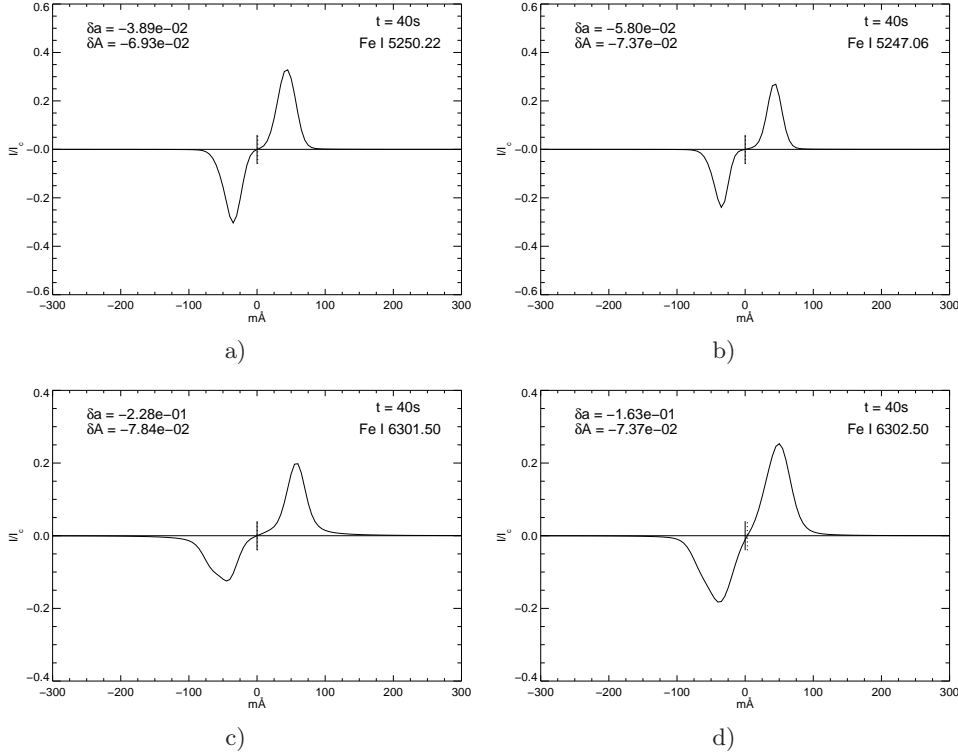


Figure 6. Stokes- V profiles of Fe I (a) λ 5250.2 Å, (b) λ 5247.06 Å, (c) λ 6301.5 Å, and (d) λ 6302.5 Å at an elapsed time of 40 s from vertical lines-of-sight in a slice ranging from $x = 410$ km to $x = 610$ km (left of the axis). The magnetic flux sheet has a field strength of 1000 G on the axis at $z = 0$. The solid vertical line marks the unshifted central wave-length position, the dotted line the zero-crossing position of Stokes- V .

The line depression contribution functions for the four Fe I lines are plotted in Fig. 8 for the initial model with moderate field strength and for the line of sight at $x = 520$ km, *i.e.*, in the center of the bundle of lines-of-sight that was considered in Fig. 6. Figure 8a shows the Stokes- I line depression contribution functions in the line cores and Fig. 8b shows the Stokes- V line depression contribution functions at the wavelength position of minimal V signals at $\lambda_{V_{\min}}$. For the definition of the Stokes line depression contribution function we refer to [Grossmann-Doerth, Larsson, and Solanki \(1988a\)](#). Clearly, the maximum contribution to both Stokes- I and Stokes- V comes for the doublet Fe I 5250.22 Å and Fe I 5247.05 Å from higher layers in the atmosphere compared to Fe I 6301.50 Å and Fe I 6302.50 Å.

The asymmetry in the Stokes- V profiles after 40 s can be clearly seen in the Fe I 6301.5 and 6302.5 Å lines plotted in Figs. 6 and 7. The effect of the wave propagation is first sensed by these lines as they are formed lower in the atmosphere than the other two lines. The Stokes- V asymmetries as a function of time for the above four lines give a clearer picture. Figure 9 shows (a) the Stokes- V amplitude asymmetry and (b) the Stokes- V area asymmetry for the four Fe I lines as a function of time. The red and blue colours represent the narrow bundles of lines-of-sight on the two sides of the

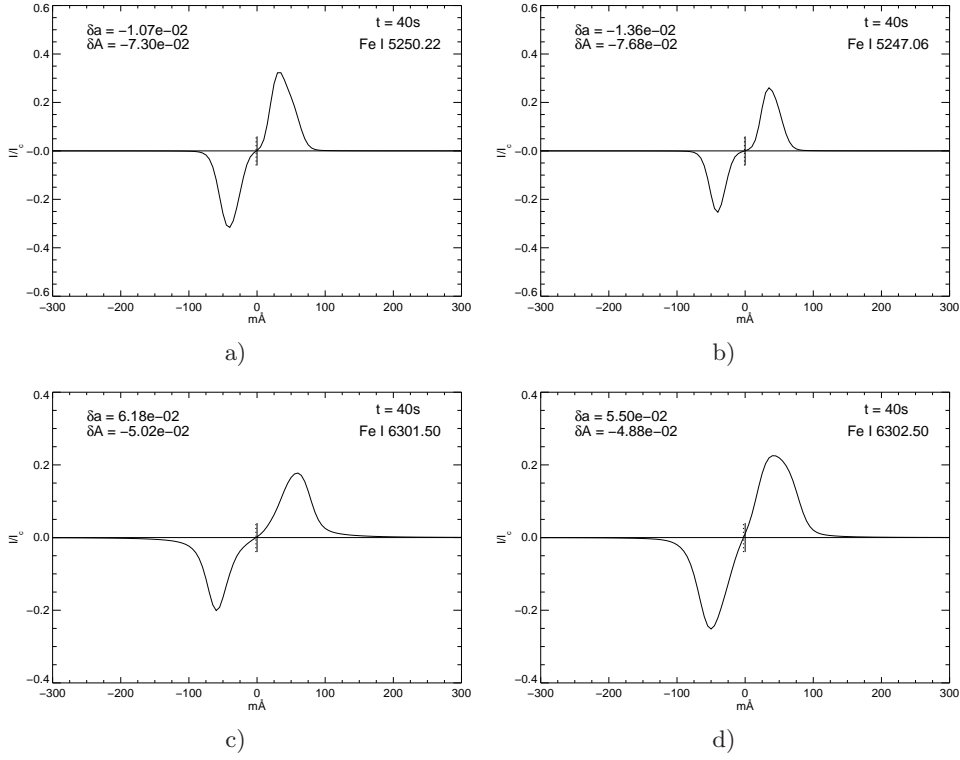


Figure 7. Stokes- V profiles of Fe I (a) λ 5250.2 Å, (b) λ 5247.06 Å, (c) λ 6301.5 Å, and (d) λ 6302.5 Å at an elapsed time of 40 s from vertical lines-of-sight in a slice ranging from $x = 670$ km to $x = 870$ km (right of the axis). The magnetic flux sheet has a field strength of 1000 G on the axis at $z = 0$. The solid and dotted vertical lines are as in Fig. 6.

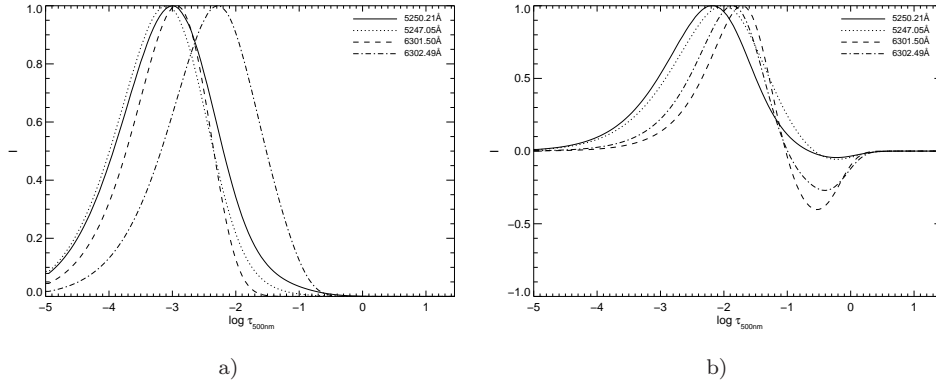


Figure 8. The line depression contribution function for the four Fe I lines of Table 2, evaluated for a line of sight located at $x = 520$ km, in the initial model with 1000 G field strength at $z = 0$ km. (a) Line depression contribution function for Stokes- I in the line core. (b) Corresponding contribution functions for Stokes- V at $\lambda = \lambda_{V_{\min}}$, *i.e.*, the wavelength of the blue Stokes- V peak.

flux-sheet axis. The blue solid curves correspond to lines-of-sight spanning $x = 410$ km to $x = 610$ km (left) and the blue dashed curves for $x = 120$ km to $x = 320$ km (far left). Similarly on the right side, the red solid curves are for $x = 670$ km to $x = 870$ km (right) and the red dashed curves are for $x = 960$ km to $x = 1160$ km (far right). In order to explain Fig. 9, it is essential to look at the velocity field of the simulation, which is shown in Fig. 4. There, the vertical lines mark the boundaries of the line-of-sight bundles.

5.1.1. Amplitude Asymmetry

Initially, there are no velocities inside the domain and hence the Stokes profiles are antisymmetric and therefore δa is zero. After the start of the simulation, velocities start building up in the domain, consequently giving rise to asymmetries in the Stokes profiles. Let us now consider the bundle of lines-of-sight on the left side of the axis and the response in δa for the lines Fe I 6301.5 or 6302.5 Å as shown in Fig. 9a. After 20 s, there develops a small down-draft within the (blue) bundle of lines-of-sight in the magnetic region. This leads to a red shift of the Stokes- V profile that forms in this region, *viz.*, in the lines Fe I 6301.5 or 6302.5 Å. The spectral line emerging from the quasi static, partially field free layer further below is less effected by Doppler shifts. It causes an asymmetric illumination of the two flanks of the red shifted line contribution formed further above. This results in the blue lobe of the emerging Stokes- V profile be suppressed and consequently the amplitude asymmetry tends to become negative. The amplitude asymmetry starts decreasing and reaches a minimum at around 50 s, after which time the down-flow moves out of the line formation region and a following up-draft starts to dominate (see Fig. 4), making the blue lobe strong again and the amplitude asymmetry to rise.

On the other hand, the line of sight on the right side of the axis shows an inverse time dependence, which is expression of the fact that the waves are 180° out of phase on opposite sides of the flux-sheet axis (Section 4.1). There develops a strong up-draft within the LOS after ≈ 30 s into the simulation. It shifts the Zeeman effected line contribution to the blue relative to the line emerging from the quasi static layer below, which suppresses the red lobe of the emerging Stokes- V profile, making the amplitude asymmetry to rise towards positive values. This trend is seen until slightly after 40 s when the down-draft of a following wave phase replaces the up-draft in these regions. The maximum value is reached before the time of minimum value of $\delta a(t)$ on the left hand side because the wave on the right hand sides of the flux-sheet axis is preceding the wave on the left hand side. However, we notice that the two curves for $\delta a(t)$ are not symmetric (relative to the time axis)—the (red) curve for the right side shows initially even a slight trend towards negative values like the (blue) curve for the left side and its amplitude is smaller than that for the left side. This asymmetry is due to the fact that the excitation of the flux-sheet is asymmetric too. The flux-sheet continuously moves to the right side until it comes to a halt after 12 s and 38.2 km to the right of the initial symmetry axis (from Eq. 9). This can be seen from Fig. 4, where the blue solid and the red solid lines-of-sight sample more peripheral and more central parts of the flux-sheet, respectively. We found that the opposite temperature perturbations on opposite sides of the flux-sheet axis has only a minor effect on the behaviour of $\delta a(t)$. This is also true for the transversal magnetic field component.

In the case of lines formed higher in the atmosphere, like the lines Fe I 5250.2 Å and 5247.06 Å, we see a similar behaviour like described above but with a time lag, depending on the arrival time of the perturbations. We see a delay of 9 s between the two pairs of lines corresponding to roughly a distance of 58 km, since the sound speed at these height is around 6.5 km s^{-1} (see Tab. 1). This distance corresponds to approximately the distance in $\log \tau$ from -1.8 to -2.1 of the maximum peaks of the Stokes- V contribution functions for the two line pairs as can be seen from Fig. 8b.

We now consider the LOSs further away from the flux-sheet axis. These are depicted as dashed vertical lines in Fig. 4 and the dashed curves in Fig. 9a show the corresponding response in δa . The perturbations become significant in this region after 50 s only when the first front arrives. On the right side of the flux-sheet, we see that the velocities are directed upward. This suppresses the red lobe making the amplitude asymmetry positive. On the left side of the flux-sheet, the downward velocities shifts the amplitude asymmetry towards negative values. We notice, however, that initially there exists the opposite tendency: especially the right side showing negative δa . This behaviour is even more pronounced for the inner bundles of lines-of-sight on the right hand side and corresponding red solid curves of Fig. 9a. It indicates that the above provided explanation for the origin of the asymmetries is not complete even though it can serve as a rough guideline. The origin of this tendency to opposite asymmetries is, that prior to the wave affecting the formation of Stokes- V , it affects the field-free layers below, where Stokes- I is already forming. In particular, the updraft in the leading wave on the right hand side first causes Stokes- I to be blue shifted, which suppresses the blue lobe of Stokes- V formed higher up in the magnetic region, which is not yet affected by the wave. This causes δa to become negative. Since the velocities are still moderate at this stage, the asymmetry remains moderate as well. As the wave moves further up it grows in amplitude and enters the magnetic region in the stripe of lines-of-sight on the far right side. This leads to a blue shift of the Stokes- V contribution, while the velocities in the field-free layer below are decreasing as the wave moves out of this region. Hence, the red lobe of Stokes- V gets suppressed. Not until then, δa rises to the expected positive values and these values become substantial because the velocities are growing rapidly.

5.1.2. Area Asymmetry

The gradients in velocity and magnetic field cause the asymmetry. A rule to calculate the sign of the area asymmetry, δA , for a purely longitudinal component has been provided by Solanki and Pahlke (1988) (see also Steiner, 1999):

$$\frac{d|B(\tau)|}{d\tau} \cdot \frac{dv(\tau)}{d\tau} \begin{cases} < 0 & \Rightarrow \delta A > 0, \\ > 0 & \Rightarrow \delta A < 0. \end{cases} \quad (13)$$

By convention, $v(\tau)$ is taken to be positive for flows in direction of increasing optical depth and *vice versa*, where v is the line-of-sight velocity. In case of a flux tube expanding with height, a LOS along the tube axis will have $d|B(\tau)|/d\tau > 0$. Given this information, together with Eq. (13), the correct interpretation of the time dependence of δA would be relatively straightforward, except that for a propagating wave the term $dv(\tau)/d\tau$ changes sign for each half wave. If the line of sight is eccentric, it may

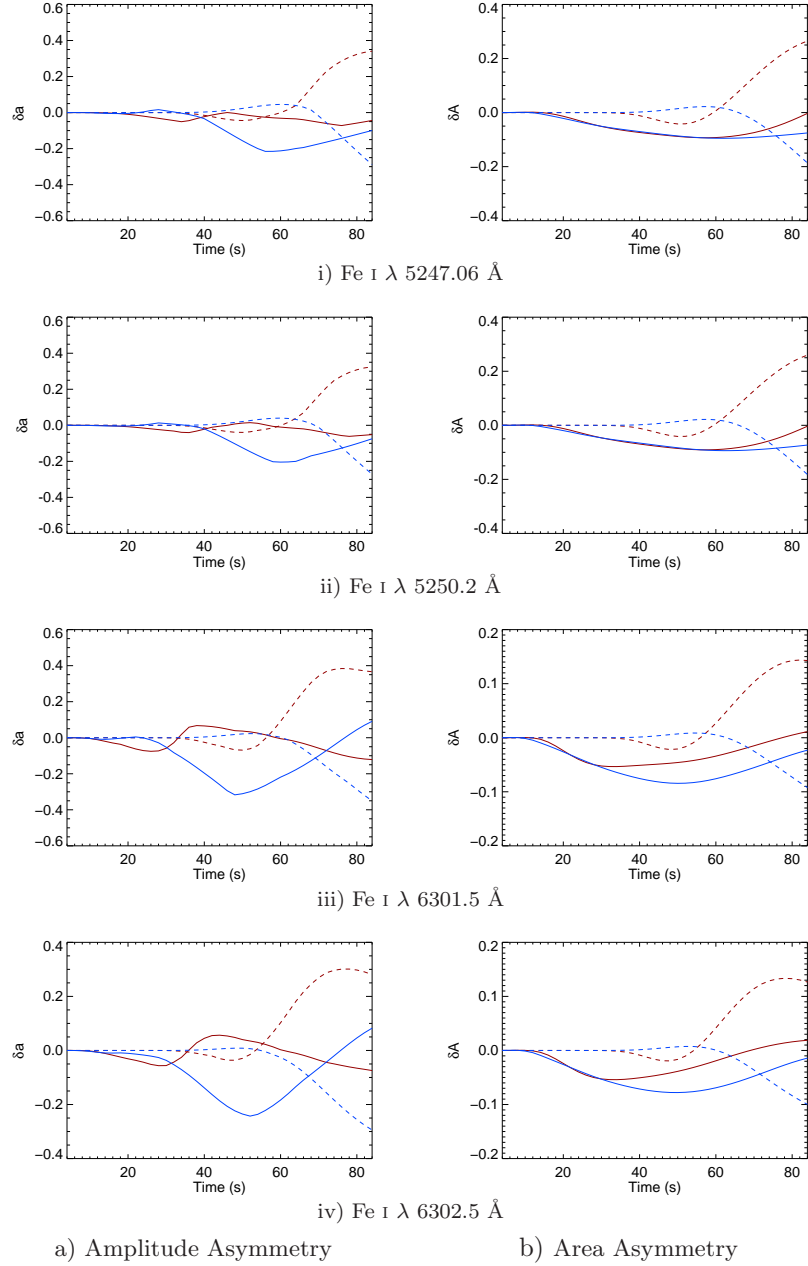


Figure 9. The Stokes- V (a) amplitude asymmetry and (b) area asymmetry for the four Fe I lines listed in Tab. 1 as a function of time for the moderate field case with 1000 G. The red solid curves represent the bundle of lines-of-sight on the right side of the the axis. The red dashed curves represent the bundle of lines-of-sight on the far right. The blue solid curves are for the left slice and blue dashed curves are for the far left bundle.

traverse the flux-sheet boundary, where the field drops suddenly with increasing optical depth, so that $d|B(\tau)|/d\tau < 0$. In this case, a positive δA is realized if $dv(\tau)/d\tau > 0$, *i.e.*, if there is an accelerating down-flow. This is for instance the case when there is no velocity inside the flux-sheet but a down-flow in the field-free surrounding region, or in case with an up-flow within the flux-sheet and no flow in the outside field-free region (Grossmann-Doerth, Schüssler, and Solanki, 1988b). Thus, $\delta A(t)$ in Fig. 9b has contributions from gradients in magnetic field and velocity that stem from inside the magnetic flux sheet as well as from the boundary of the flux-sheet. These contributions may have opposite sign. This is also true for contributions from different phases of the wave. In addition, δA is an integral quantity with contributions over all wavelength of the spectral line. Hence, δA forms over a wide height range and therefore includes more than a single wave crest or wave trough. This renders the correct interpretation of $\delta A(t)$ in this case more intricate than it is for $\delta a(t)$. This is in particular true for the inner bundles of lines-of-sight. The outer bundles show a behaviour very similar to that of $\delta a(t)$.

5.2. Strong Field Case

The emergent Stokes- V profiles were also computed for a flux-sheet with a magnetic field strength of 1600 G on the axis at $z = 0$ km. Of the two cases shown in Fig. 5, we consider in the following only the case with the wide excitation region. When spatially averaging these profiles over the entire width of the box, they do not show significant variation with time, revealing no sign of wave propagation inside the box, similar to the case with a field strength of 1000 G. Profiles averaged over smaller slices on either side of the axis show signs of wave propagation, once again emphasizing that lines-of-sight that are placed away from the symmetry axis of the flux-sheet yield more information about the wave activity. Here, we carry out a similar study of the evolution of the Stokes- V asymmetries for the 1600 G case as was done for the moderate field case. Figs. 10 and 11 show the Stokes- V profiles at time $t = 50$ s of the four Fe I lines under study. Figure 10 shows the Stokes- V profiles averaged over a horizontal range from $x = 120$ km to $x = 320$ km (far left bundle of lines-of-sight) and Fig. 11 shows the profiles averaged over a range from $x = 960$ km to $x = 1160$ km (far right bundle of lines-of-sight).

The Stokes- V amplitude asymmetry and area asymmetry as a function of time for these lines are shown in Fig. 12. The colour coding is the same as in Fig. 9. The temperature perturbation and the velocity field for different time instances is shown in Fig. 5b. There, the colours represent the value of ΔT and the arrows show the velocity vectors at times $t = 20, 30, 40,$ and 50 s.

Unlike the case with 1000 G, here we have significant fast, predominantly magnetic waves, which get refracted within the flux-sheet and convert to fast acoustic waves when they encounter the flux-sheet boundary, where they leave the flux-sheet and enter the field-free domain. This causes the wing-like feature in the temperature perturbations of Fig. 5b that extends from $z = 300$ km to $z = 700$ km on both sides of the flux-sheet (approximately along the $\beta = 1$ contour) at time $t = 40$ s. The velocities associated with both the fast and the slow wave results in the shift and the asymmetries of the Stokes- V profiles.

In the following, we consider a bundle of lines-of-sight on the far right side of the flux-sheet axis. Here, the front of the fast, predominantly magnetic wave starts to become

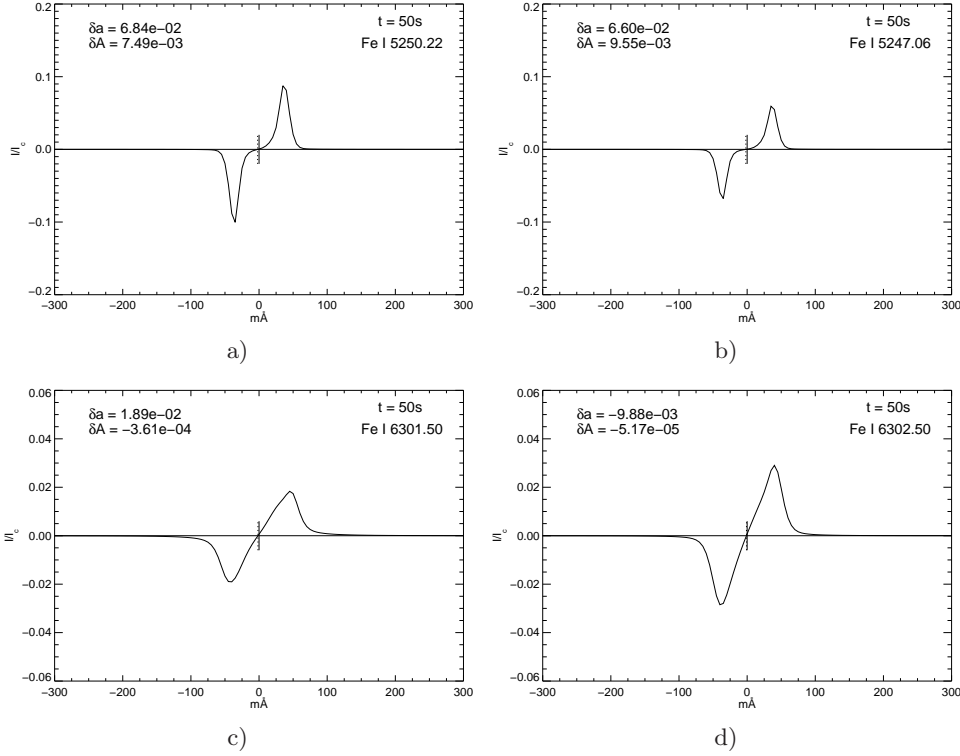


Figure 10. Stokes- V profiles of Fe I (a) λ 5250.2 Å, (b) λ 5247.06 Å, (c) λ 6301.5 Å, and (d) λ 6302.5 Å at an elapsed time of 50 s from vertical lines-of-sight in a slice ranging from $x = 120$ km to $x = 320$ km (far left of the axis). The magnetic flux sheet has a field strength of 1600 G on the axis at $z = 0$. The solid and dotted vertical lines are as in Fig. 6.

effective at a $t \approx 40$ s. The velocities are directed downwards in the magnetic region, resulting in a red shifted Stokes- V contribution illuminated by light from the unshifted absorption formed in the static layer below, which suppresses the blue lobe, leading to a negative asymmetry (dashed red curve in Fig. 12a). At $t = 60$ s, this down-flow has moved out of the LOS bundle into the field-free region while within the magnetic region a up-flow evolves. This up-flow, which is due to the following slow mode, gives rise to a positive asymmetry leading to a strong positive bump of the red dashed curve around $t = 70$ s. This behaviour is different from the 1000 G case shown in Fig. 9a wherein the first negative bump due to the fast converting mode is less pronounced or missing because of the relatively weak magnetic field. The LOS on the left hand side of the flux-sheet axis shows a similar behaviour but of opposite sign. This behaviour can also be seen in the area asymmetry of the outer bundles of lines-of-sight. Thus, δa and δA show a clear signature of both the fast and the slow mode.

5.2.1. Zero-Crossing Shift

The flows within the magnetic elements can be estimated by the Stokes- V zero-crossing shift, given by Eq. (10). The 180° out of phase flow pattern formed on the two sides of

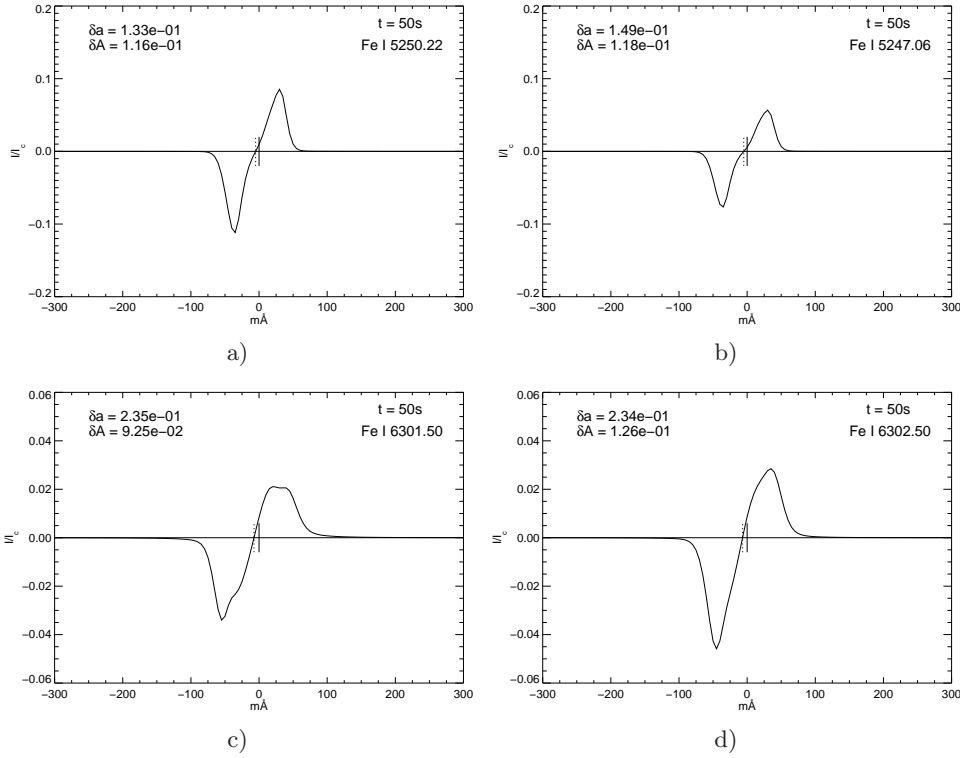


Figure 11. Stokes- V profiles of Fe I (a) λ 5250.2 Å, (b) λ 5247.06 Å, (c) λ 6301.5 Å, and (d) λ 6302.5 Å at an elapsed time of 50 s from vertical lines-of-sight in a slice ranging from $x = 960$ km to $x = 1160$ km (far right of the axis). The magnetic flux sheet has a field strength of 1600 G on the axis at $z = 0$. The solid and dotted vertical lines are as in Fig. 6.

the flux-sheet axis creates phase shifted, opposite zero-crossing shifts in both magnetic field models. Figure 13 shows the Stokes- V zero-crossing shift as a function of time for the moderate and the strong field cases. In case of moderate field LOS bundles close to the sheet axis, the up-flow on the right side and the down-flow on the left side of the axis, which stem from the respective compressional and rarefactional front of the slow (acoustic) wave, results in a net zero-crossing shift of opposite behaviour on either side. The curves are shifted in time for the four lines and the two LOS bundles due to the difference in the formation heights of the lines and due to the time lag of the waves to the left and to the right of the flux-sheet axis, respectively. A similar trend in the zero-crossing shift can be seen in the outer LOS bundles, where the wave fronts arrive later. The flow pattern associated with the fast (magnetic) wave is a prominent feature in the case with the strong field. It creates the significant bump of opposite sign on either side of the flux-sheet for the outer LOS bundles around $t \approx 40$ s, visible in the dashed curves of Fig. 13b.

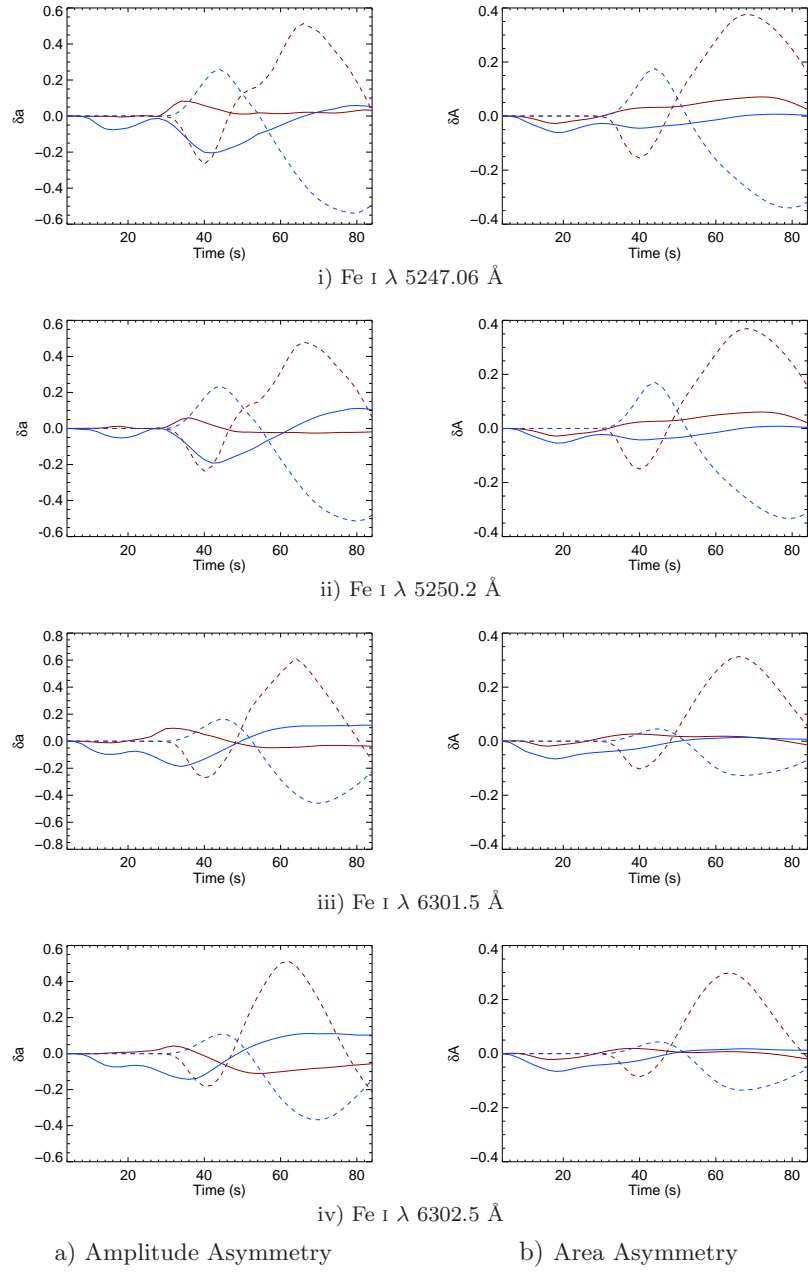


Figure 12. The Stokes- V (a) amplitude asymmetry and (b) area asymmetry for the four Fe I lines as a function of time for the strong field case with 1600 G. The red solid curves represent the right side of the flux-sheet axis. The red dashed curves represent the bundle on the far right. Blue solid curves are for the left bundle and the blue dashed curves are for the far left bundle.

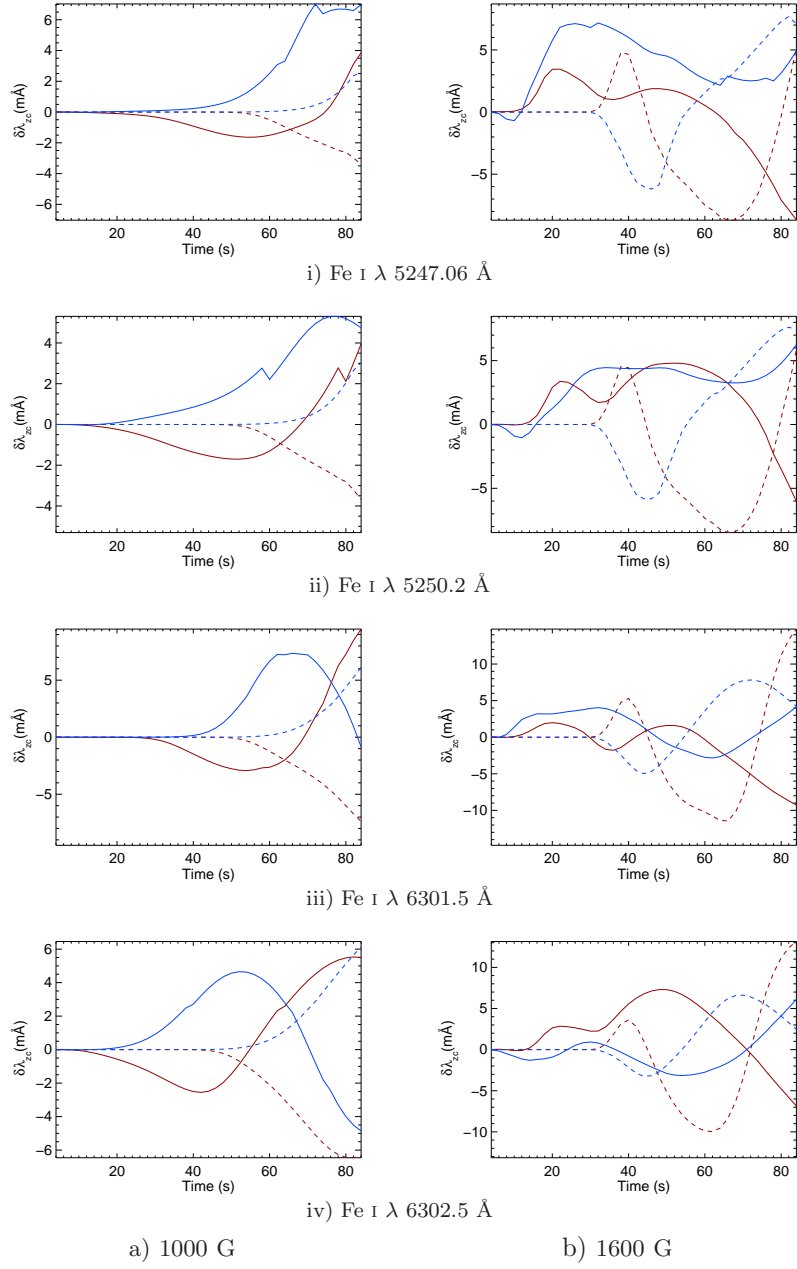


Figure 13. Stokes- V zero-crossing shift for the four Fe I lines as a function of time for (a) the moderate field case with 1000 G and (b) the strong field case with 1600 G. The red solid curves represent the slice on the right side of the axis. The red dashed curves represent the slice on the far right. Blue solid curves are for the left slice and the blue dashed curves are for the far left slice.

6. Summary and Conclusion

This work is an extension of a previous work by [Vigeesh, Hasan, and Steiner \(2009\)](#), which focussed on the dynamics and the energy transport that occur in intense flux tubes. In the present work, we have constructed flux tubes embedded in the photosphere and used the results of our simulation to compute the Stokes profiles that emerge from the top of the simulation box in order to study observational signatures of wave propagation inside the tubes.

The nature of the excited modes depends on the value of plasma β at the place where the driving motion occurs. Depending upon the extent of the region of excitation, energy imparted to the different modes vary. When the excitation occurs in a high- β plasma, we observe that the excited modes are a slow acoustic wave and a fast magnetic wave that undergo mode conversion and transmission across the $\beta = 1$ layer. In the case of excitation of a low- β flux-sheet over a large enough impact area, most of the energy will go to the fast (magnetic) mode. If the area of impact is smaller, then most of the energy goes into the slow (acoustic) wave, which is channeled up along the flux tube and eventually dissipates by shock formation. Hence, the impact of a large granules may impart more energy to the fast (magnetic) mode, but the non-magnetic atmosphere gains back this energy in the form of a fast (acoustic) wave due to refraction of the fast mode and mode conversion.

The antisymmetry in the wave pattern with respect to the flux-sheet axis gives rise to observational signatures. While the average Stokes- V profile over the whole domain does not show any significant variation with time, clear evidence of the wave phenomena can be detected when looking at higher resolved lines-of-sight on either side of the flux-sheet. Stokes- V profiles become asymmetric, showing opposite temporal behaviour on the two sides of the flux-sheet axis. Furthermore, effects of refraction of the fast, predominantly magnetic wave in the case of a strong magnetic field are clearly visible in the Stokes asymmetry and zero-crossing shift as a function of time. Our results show a clear signature of the fast, predominantly magnetic wave in these profiles. We come to the conclusion that polarimetric signatures of wave propagation in magnetic elements can be observed, provided that the spatial resolution is high enough so that magnetic concentrations can be resolved into different regions within the flux concentration. Although, the simulated Stokes asymmetries would be detectable with current polarimetric instruments, observations of considerably higher spatial resolution, capable of resolving individual flux concentrations, are needed in order to reveal the propagation of waves in individual flux concentrations and to detect the different modes of the MHD waves. We have highlighted the importance of using the Stokes- V asymmetries as a possible diagnostic tool to study wave propagation in magnetic elements at disk center. Observations off disk center would possibly slightly relax the high requirements of spatial resolution because the wave pattern can be expected to be less antisymmetric in this case. However, the interpretation of the polarimetric signals as a function of time would become more intricate. The analysis in this work is based on photospheric lines under the assumption of local thermodynamic equilibrium (LTE). Hence our conclusions are not valid for lines formed in the chromosphere, since LTE approximation is no longer valid in this region. A more realistic modelling should be carried out in three spatial dimensions and include NLTE effects.

Acknowledgements This work was supported by the German Academic Exchange Service (DAAD), grant D/05/57687, and the Indian Department of Science and Technology (DST), grant DST/INT/DAAD/P146/2006.

References

- Bogdan, T.J., Carlsson, M., Hansteen, V.H., McMurphy, A., Rosenthal, C.S., Johnson, M., Petty-Powell, S., Zita, E.J., Stein, R.F., McIntosh, S.W., Nordlund, Å.: 2003, Waves in the Magnetized Solar Atmosphere. II. Waves from Localized Sources in Magnetic Flux Concentrations. *Astrophys. J.* **599**, 626–660. doi:[10.1086/378512](https://doi.org/10.1086/378512).
- Cally, P.S.: 2007, What to look for in the seismology of solar active regions. *Astronomische Nachrichten* **328**, 286. doi:[10.1002/asna.200610731](https://doi.org/10.1002/asna.200610731).
- Cranmer, S.R., van Ballegoijen, A.A.: 2005, On the Generation, Propagation, and Reflection of Alfvén Waves from the Solar Photosphere to the Distant Heliosphere. *Astrophys. J. Suppl.* **156**, 265–293. doi:[10.1086/426507](https://doi.org/10.1086/426507).
- Fedun, V., Erdélyi, R., Shelyag, S.: 2009, Oscillatory Response of the 3D Solar Atmosphere to the Leakage of Photospheric Motion. *Solar Phys.* **258**, 219–241. doi:[10.1007/s11207-009-9407-9](https://doi.org/10.1007/s11207-009-9407-9).
- Fujimura, D., Tsuneta, S.: 2009, Properties of Magnetohydrodynamic Waves in the Solar Photosphere Obtained with Hinode. *Astrophys. J.* **702**, 1443–1457. doi:[10.1088/0004-637X/702/2/1443](https://doi.org/10.1088/0004-637X/702/2/1443).
- Grossmann-Doerth, U.: 1994, Height of formation of solar photospheric spectral lines. *Astron. Astrophys.* **285**, 1012–1018.
- Grossmann-Doerth, U., Larsson, B., Solanki, S.K.: 1988a, Contribution and response functions for Stokes line profiles formed in a magnetic field. *Astron. Astrophys.* **204**, 266–274.
- Grossmann-Doerth, U., Schüssler, M., Solanki, S.K.: 1988b, Unshifted, asymmetric Stokes V-profiles - Possible solution of a riddle. *Astron. Astrophys.* **206**, L37–L39.
- Grossmann-Doerth, U., Schüssler, M., Steiner, O.: 1998, Convective intensification of solar surface magnetic fields: results of numerical experiments. *Astron. Astrophys.* **337**, 928–939.
- Hasan, S.S., van Ballegoijen, A.A.: 2008, Dynamics of the Solar Magnetic Network. II. Heating the Magnetized Chromosphere. *Astrophys. J.* **680**, 1542–1552. doi:[10.1086/587773](https://doi.org/10.1086/587773).
- Hasan, S.S., van Ballegoijen, A.A., Kalkofen, W., Steiner, O.: 2005, Dynamics of the Solar Magnetic Network: Two-dimensional MHD Simulations. *Astrophys. J.* **631**, 1270–1280. doi:[10.1086/432655](https://doi.org/10.1086/432655).
- Kato, Y., Steiner, O., Steffen, M., Suematsu, Y.: 2011, Excitation of Slow Modes in Network Magnetic Elements Through Magnetic Pumping. *Astrophys. J. Lett.* **730**, L24. doi:[10.1088/2041-8205/730/2/L24](https://doi.org/10.1088/2041-8205/730/2/L24).
- Khomenko, E., Collados, M., Felipe, T.: 2008, Nonlinear Numerical Simulations of Magneto-Acoustic Wave Propagation in Small-Scale Flux Tubes. *Solar Phys.* **251**, 589–611. doi:[10.1007/s11207-008-9133-8](https://doi.org/10.1007/s11207-008-9133-8).
- Nave, G., Johansson, S., Learner, R.C.M., Thorne, A.P., Brault, J.W.: 1994, A new multiplet table for Fe I. *Astrophys. J. Suppl.* **94**, 221–459. doi:[10.1086/192079](https://doi.org/10.1086/192079).
- Pietarila, A., Socas-Navarro, H., Bogdan, T., Carlsson, M., Stein, R.F.: 2006, Simulation of quiet-sun waves in the Ca II infrared triplet. *Astrophys. J.* **640**, 1142–1152. doi:[10.1086/500240](https://doi.org/10.1086/500240).
- Rosenthal, C.S., Bogdan, T.J., Carlsson, M., Dorc, S.B.F., Hansteen, V., McIntosh, S.W., McMurphy, A., Nordlund, Å., Stein, R.F.: 2002, Waves in the Magnetized Solar Atmosphere. I. Basic Processes and Internetwork Oscillations. *Astrophys. J.* **564**, 508–524. doi:[10.1086/324214](https://doi.org/10.1086/324214).
- Shelyag, S., Mathioudakis, M., Keenan, F.P., Jess, D.B.: 2010, A photospheric bright point model. *ArXiv e-prints*.
- Sigwarth, M.: 2000, Dynamics of Solar Magnetic Fields – A Spectroscopic Investigation. In: Schieler, R.E. (ed.) *Reviews in Modern Astronomy, Reviews in Modern Astronomy* **13**, 45.
- Socas-Navarro, H., Borrero, J.M., Asensio Ramos, A., Collados, M., Domínguez Cerdeña, I., Khomenko, E.V., Martínez González, M.J., Martínez Pillet, V., Ruiz Cobo, B., Sánchez Almeida, J.: 2008, Multiline Spectropolarimetry of the Quiet Sun at 5250 and 6302 Å. *Astrophys. J.* **674**, 596–606. doi:[10.1086/521418](https://doi.org/10.1086/521418).
- Solanki, S.K., Pahlke, K.D.: 1988, Can stationary velocity fields explain the Stokes V asymmetry observed in solar magnetic elements? *Astron. Astrophys.* **201**, 143–152.
- Steiner, O.: 1999, Flux Tube Dynamics. In: Schmieder, B., Hofmann, A., Staude, J. (eds.) *Third Advances in Solar Physics Euroconference: Magnetic Fields and Oscillations, Astronomical Society of the Pacific Conference Series* **184**, 38–54.

- Steiner, O.: 2007, Photospheric processes and magnetic flux tubes. In: S. S. Hasan & D. Banerjee (ed.) *Kodai School on Solar Physics, American Institute of Physics Conference Series* **919**, 74–121. doi:[10.1063/1.2756784](https://doi.org/10.1063/1.2756784).
- Steiner, O., Knölker, M., Schüssler, M.: 1994, Dynamic interaction of convection with magnetic flux sheets: first results of a new MHD code. In: Rutten, R.J., Schrijver, C.J. (eds.) *Solar Surface Magnetism*, 441.
- Steiner, O., Pneuman, G.W., Stenflo, J.O.: 1986, Numerical models for solar magnetic fluxtubes. *Astron. Astrophys.* **170**, 126–137.
- Steiner, O., Grossmann-Doerth, U., Knölker, M., Schüssler, M.: 1998, Dynamical Interaction of Solar Magnetic Elements and Granular Convection: Results of a Numerical Simulation. *Astrophys. J.* **495**, 468. doi:[10.1086/305255](https://doi.org/10.1086/305255).
- Stenflo, J.O.: 1994, *Solar Magnetic Fields: Polarized Radiation Diagnostics*.
- Vigeesh, G., Hasan, S.S., Steiner, O.: 2009, Wave propagation and energy transport in the magnetic network of the Sun. *Astron. Astrophys.* **508**, 951–962. doi:[10.1051/0004-6361/200912450](https://doi.org/10.1051/0004-6361/200912450).

